Available online at www.sciencedirect.com

ScienceDirect

Ceramics International 37 (2011) 1359–1365

CERAMICS INTERNATIONAL

www.elsevier.com/locate/ceramint

Dependence of optical properties on doping metal, crystallite size and defect concentration of M-doped ZnO nanopowders (M = Al, Mg, Ti)

Sumetha Suwanboon [a,*], Pongsaton Amornpitoksuk [b], Apinya Sukolrat [c]

[a] Department of Materials Science and Technology, Faculty of Science, Prince of Songkla University, Hat Yai, Songkhla 90112, Thailand
[b] Department of Chemistry and Center for Innovation in Chemistry, Faculty of Science,
Prince of Songkla University, Hat Yai, Songkhla 90112, Thailand
[c] Scientific Equipment Center, Prince of Songkla University, Hat Yai, Songkhla 90112, Thailand

Received 26 October 2010; received in revised form 8 November 2010; accepted 16 December 2010
Available online 21 January 2011

Abstract

ZnO, Al-, Mg- and Ti-doped ZnO nanopowders were synthesized from CTAB-assisted oxalate intermediate by thermal decomposition method at 600 °C in air. All samples presented a hexagonal wurtzite structure. The spherical nanoparticles assembled in a porous octahedron-like shape for all samples. The size of Al-doped ZnO nanopowders increased as a function of Al ion concentration whereas the size of Mg- and Ti-doped ZnO nanopowders decreased when Mg and Ti ion concentrations were increased. The increment and reduction of their sizes can be explained by the Zener pinning effect. The E_g value of Al-doped ZnO nanopowders slightly decreased when Al ions were increased due to the crystallite size and defect concentration increased. In contrast, the E_g value of Mg- and Ti-doped ZnO nanopowders increased as a function of Mg and Ti ion concentration which can be explained by the Moss–Burstein effect.

Keywords: A. Powders: chemical preparation; B. Defects; C. Optical properties; D. ZnO

1. Introduction

For almost a decade, nanomaterials have been attracting interest in the world of science. Great efforts have been recently devoted to the preparation of nanostructured metal oxides with a variety of shapes and sizes, because of their strikingly uncommon properties [1–5]. Among the nanostructured metal oxides, ZnO is considered to be one of the best metal oxides that can be used at a nanoscale level. ZnO itself has normally a hexagonal or wurtzite structure and it is well-known as an n-type II–VI semiconductor with a wide direct band-gap of about 3.37 eV and a large exciton binding energy of 60 meV [6]. From this point of view, nanostructured ZnO powders display a great power in many applications such as gas sensors [7], solar cells [8], varistors [9] and photocatalyst with high chemical activity [10]. A number of chemical methods of synthesis have been applied to synthesize nanostructured ZnO powders, for example by using hydrothermal [11], precipitation [6], sol–gel [12] and thermal decomposition [13] methods. Among these chemical routes, precipitation and thermal decomposition are a common method that can be used for large scale production. Moreover, the particle shape can be controlled easily by modifying the precursor solution with an appropriate surfactant such as diethylene glycol (DEG) [14], cetyltrimethylammonium bromide (CTAB) [15], sodium dodecyl sulfate (SDS) [16], monoethanolamine (MEA), diethanolamine (DEA) or triethanolamine (TEA) [17]. To date, a number of research workers have reported the fabrication of nanostructured ZnO powders with spherical [14], rod-like [18], flower-like [10] and sheet-like [19] structures. Only a few reports [11,20,21] have involved the synthesis of porous ZnO through an oxalate intermediate by a chemical route. Likewise only a few researchers have investigated the construction of porous metal-doped ZnO powders, for example, Peiteado et al. [22] studied the phase formation of a $Zn_{1-x}Mn_xO$ system. Kanade et al. [23] reported the formation of self-assembled aligned Cu-doped ZnO nano-

---

* Corresponding author. Tel.: +66 74 28 82 50; fax: +66 74 28 83 95.
E-mail address: ssuwanboon@yahoo.com (S. Suwanboon).

0272-8842/$36.00 © 2011 Elsevier Ltd and Techna Group S.r.l. All rights reserved.
doi:10.1016/j.ceramint.2010.12.010

particles for photocatalytic hydrogen production under visible light irradiation. Astonishingly enough, the publication concerning porous Al-, Mg- and Ti-doped ZnO nanopowders was still incomplete. Therefore, a synthesis of porous Al-, Mg- and Ti-doped ZnO nanopowders via the oxalate precursor by thermal decomposition method in the presence of CTAB could be worthwhile investigating.

In this paper, we report the influence of a small amount of Al, Mg and Ti ion concentrations in the precursor solution modified with CTAB on the self-assembled aligned Al-, Mg- and Ti-doped ZnO nanopowders and we also report the effects of Al, Mg and Ti ion concentration on the crystallite size, defect concentration and optical properties.

2. Experimental

Firstly, 0.16 mol $C_2H_2O_4{\cdot}2H_2O$ (oxalic acid) was dissolved in 100 ml of distilled water with vigorous stirring and 0.02 mol CTAB was then added until a homogeneous $CTAB/C_2H_2O_4{\cdot}2H_2O$ solution was obtained. Secondly, 0.02 mol $Zn(NO_3)_2{\cdot}6H_2O$ was dissolved in 100 ml of distilled water and various amounts of $AlCl_3{\cdot}6H_2O$, $MgCl_2{\cdot}4H_2O$ or $TiCl_4$ were added to obtain 1, 3 and 5 mol% Al, Mg or Ti ions in the solutions. Finally, the mixtures of $Zn(NO_3)_2{\cdot}6H_2O$ and the doping agent was each slowly added into the aqueous $CTAB/C_2H_2O_4{\cdot}2H_2O$ solution. White precipitates were formed and the suspensions were continuously stirred at room temperature for 1 h, and then filtered, washed with distilled water several times and ethanol, dried at room temperature and calcined at 600 °C in air for 1 h.

The phase formation was determined by an X-ray diffraction (XRD, X'Pert MPD). The morphology of the dried samples was observed by a scanning electron microscope (SEM, JSM-5800LV, JEOL). The elemental analysis was carried out by an energy dispersive spectroscopy (EDS, Oxford ISIS 300). Diffuse refractance spectra (DRS) were recorded by a UV–vis spectrophotometer using $BaSO_4$ as reference (UV-2401, Shimadzu). The thermal evolution of a representative sample was carried out by a thermogravimetric analysis (TGA7, Perkin Elmer) and a differential thermal analysis (DTA7, Perkin Elmer) under a nitrogen atmosphere at a heating rate of 10 °C/min.

3. Results and discussion

3.1. Characterization

3.1.1. Thermal analysis

Thermal decomposition of an as-prepared sample was verified by the thermogravimetric analysis and the result is presented in Fig. 1. The TGA curve showed two weight losses. The first weight loss occurred at a temperature of between 90 and 180 °C, which corresponded to the loss of two water molecules from the zinc oxalate dihydrate to form anhydrous zinc oxalate [24].

$$ZnC_2O_4 \cdot 2H_2O \xrightarrow{90-180\,^{\circ}C} ZnC_2O_4 + 2H_2O$$

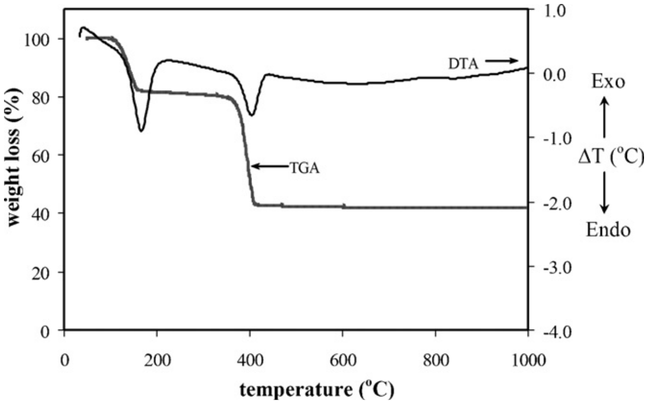

Fig. 1. TGA and DTA spectra of an as-prepared undoped-ZnO sample.

The second weight loss occurred at a temperature of between 375 and 450 °C, which was attributed to the conversion of anhydrous zinc oxalate to zinc oxide.

$$ZnC_2O_4 \xrightarrow{375-450\,^{\circ}C} ZnO + CO_2$$

The DTA result also showed two sharp endothermic peaks at temperatures of about 116 and 375 °C that corresponded to the weight losses in the TGA curve.

3.1.2. X-ray diffraction studies

The phase formation was revealed by the XRD technique. Fig. 2(a) shows the diffraction pattern of the as-prepared sample, it can be clearly seen that the diffraction pattern of the as-prepared sample matched the monoclinic zinc oxalate dihydrate in accordance with the JCPDS database 25-1029. Fig. 2(b) shows the diffraction patterns of the sample calcined at 600 °C in air for 1 h, the results were indexed on the basis of the hexagonal structure reported for ZnO and all peak positions agree well with the diffraction pattern of bulk ZnO (JCPDS database 36-1451) with the lattice parameters: $a = 0.3250$ nm, $c = 0.5207$ nm and space group $P6_3mc$. Therefore, it could be said that the ZnO nanopowders can form through thermal decomposition of zinc oxalate dihydrate. This result was confirmed by the obtained TGA as previously reported. In addition, Al-, Mg- and Ti-doped ZnO nanopowders were also

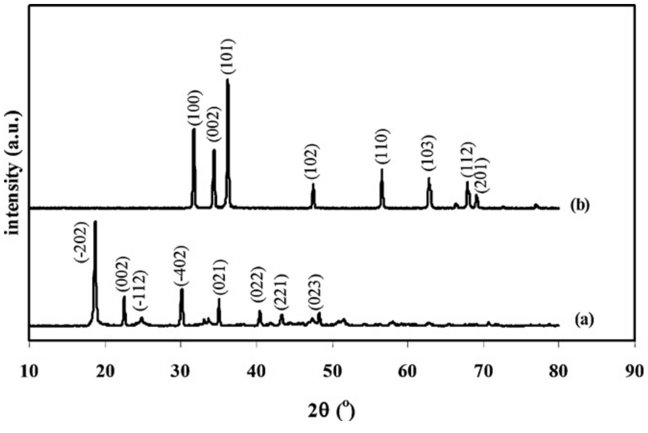

Fig. 2. XRD patterns of (a) an as-prepared undoped-ZnO sample and (b) calcined samples at 600 °C.

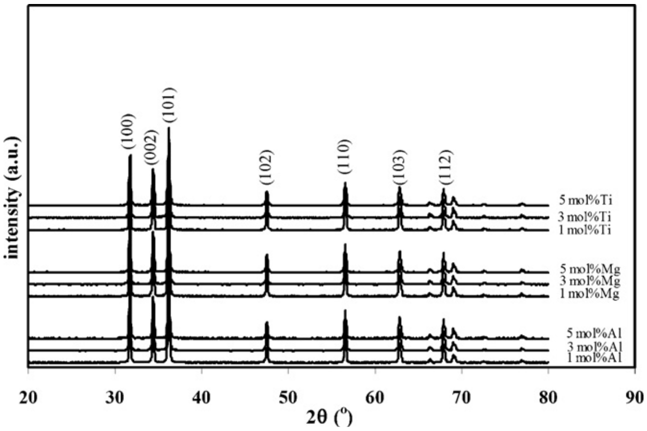

Fig. 3. XRD patterns of calcined Al-, Mg- and Ti-doped ZnO nanopowders with various concentrations of doping metal.

Table 1
Information on the ZnO samples prepared using various conditions.

Doping metal	Content (mol%)	Crystallite size (nm)	Lattice parameter (nm)		E_g (eV)	E_a
			a	c		
Pure ZnO	–	53	0.3253	0.5211	3.20	0.064
Al	1	48	0.3253	0.5212	3.20	0.080
	3	51	0.3254	0.5213	3.19	0.085
	5	56	0.3253	0.5211	3.17	0.093
Mg	1	52	0.3253	0.5212	3.20	0.076
	3	51	0.3254	0.5212	3.21	0.079
	5	45	0.3253	0.5211	3.22	0.079
Ti	1	46	0.3253	0.5211	3.20	0.071
	3	44	0.3253	0.5212	3.21	0.072
	5	39	0.3253	0.5211	3.23	0.072

investigated by the XRD technique as shown in Fig. 3. It was observed that the diffraction patterns of all Al-, Mg- and Ti-doped ZnO nanopowders were similar to the diffraction pattern of ZnO standard and it was evident that no other impurity peaks related to the metal-doped components such as Al_2O_3, MgO and TiO_2 were detected. This indicated that the doping metal ions did not change its wurtzite structure similar to the case of Sb-doped ZnO powders [25].

From the XRD analysis, the effect of Al, Mg and Ti ion concentrations in the solution on crystallite size and lattice parameters was determined. For the wurtzite structure, the lattice parameters were calculated from the relationship of the interplanar spacing of the $\{h\,k\,l\}$ plane and lattice parameters: a and c via the Miller indices $h\,k\,l$ using the following relationship:

$$\frac{1}{d_{hkl}^2} = \frac{4}{3}\left[\frac{h^2 + hk + k^2}{a^2}\right] + \frac{l^2}{c^2} \tag{1}$$

In fact, a change of lattice parameters is dependent upon the size of impurity or doping atom that can incorporate into ZnO lattice. When impurity or doping ion that has a smaller ionic radius compared to Zn ion is incorporated into ZnO lattice, their lattice parameters decrease. In contrast, when impurity or doping ion that has a larger ionic radius compared to Zn ion is incorporated into ZnO lattice, their lattice parameters increase [26]. From Table 1, the lattice parameters of Al-, Mg- and Ti-doped ZnO nanopowders are indifferent when compared to the lattice parameters of pure ZnO nanopowders, indicating that the Al, Mg and Ti ions may remain adhered to ZnO surface instead of incorporating into the ZnO lattice [27].

In this study, the effect of various doping metal ions on crystallite size was investigated and the crystallite size was calculated using the Scherrer's formula [6]:

$$D = \frac{k\lambda}{\beta\cos\theta} \tag{2}$$

where D is the average crystallite size, β is the full width at the half maximum of the diffraction peak, θ is the Bragg angle, λ is the wavelength of X-ray used and k is a constant (=1). The crystallite size systematically decreased when the concentration of Mg and Ti ions in the precursor solution was increased whereas the crystallite size slightly increased as the Al ions were increased and the crystallite size of Al-doped ZnO nanopowder was larger than that of pure ZnO when Al ion was increased to 5 mol% as reported in Table 1.

It is noteworthy that the obstacles could be introduced into ZnO structure by either a precipitation of a secondary phase or contamination at the surface of ZnO. Hence, the obstacles can prevent the growth of crystallite size or particle size by the Zener pinning effect [28]. When the moving boundaries attach to the obstacles, they, in turn, exert a retarding force on the boundary and the maximum force that may be exerted by a single particle could be expressed by following equation:

$$F_{\max} = \pi r_p \gamma_b \tag{3}$$

where γ_b is the grain boundary energy and r_p is the obstacle radius. If the number of obstacles per unit volume is f_r, then the number of obstacles per unit area is given by $3f_r/2\pi r_p^2$, and the retarding force per unit area (F_r) can be approximated by following equation:

$$F_r = \frac{3f_r\gamma_b}{2r_p} \tag{4}$$

It is well-known that the growth of particles reduces the overall energy where the average driving force (F_d) is given by:

$$F_d = \frac{\alpha\gamma_b}{r} \tag{5}$$

where r is the particle radius, γ_b is the grain boundary energy and α is a geometrical constant. Therefore, the presence of a greater retarding force produced a greater inhibition of the growth of particles. Taking into account the formula for evaluating the retarding force per unit area, the major reason for how the retarding force could be increased is the number of obstacles per unit volume (f_r). The retarding force could increase when the number of obstacles per unit volume was further adhered on the ZnO surface. For this reason, the crystallite size of Mg- and Ti-doped ZnO nanopowders decreased when Mg and Ti ions were increased. On the other hand, the crystallite size of Al-doped ZnO nanopowders increased from 48 to 56 nm when the Al ions were varied from 1 to 5 mol%, respectively. Considering the Eq. (4) again, the efficiency of the pinning reduces when the particles coarsen, giving rise to a change in the ratio of f_r/r_p as a result of an increase in r_p. Hence, the pinning under certain conditions may lead to the particle growth. In the case of Al-doped ZnO nanopowders, it was observed that the crystallite size increased as a function of Al ions concentration due to the coarsening of the doping metal.

In this study, the crystallite size of Ti-doped ZnO nanopowders was much smaller than the crystallite size of Mg-doped ZnO nanopowders. So, the elemental analysis of a representative sample was done by the EDS and it was observed that about 0.1 at.% Mg and 0.15 at.% Ti were detected in the ZnO samples when doping with 5 mol% Mg and Ti ions in the

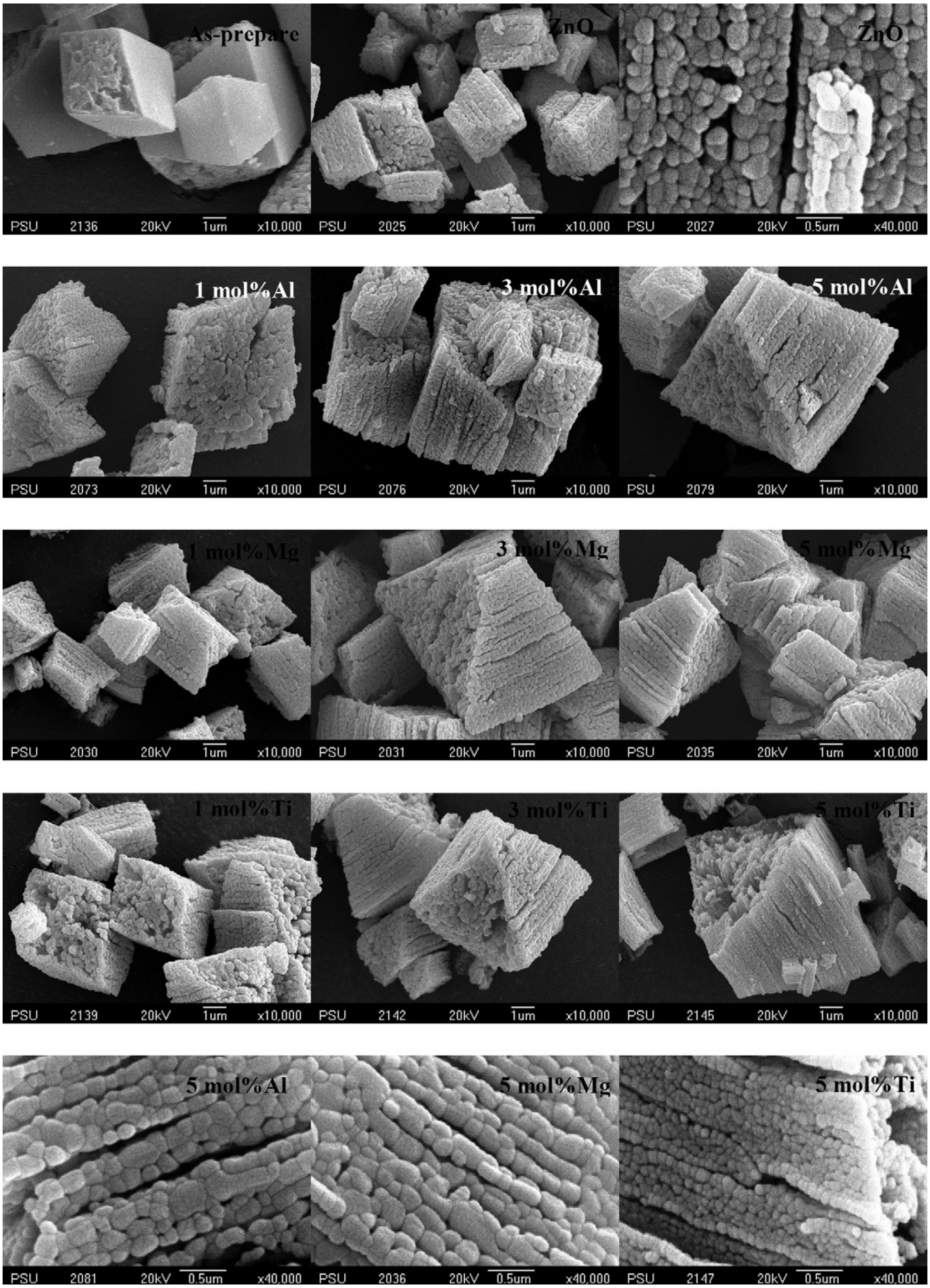

Fig. 4. SEM images of ZnO, Al-, Mg- and Ti-doped ZnO nanopowders with various concentrations of doping metal.

solutions, respectively. Therefore, the crystallite size of the Ti-doped ZnO nanopowders was smaller than that of the crystallite size of Mg-doped ZnO nanopowders because of a higher amount of obstacles on the ZnO surface.

3.1.3. Morphological study

The secondary electron images of the as-prepared and calcined samples are shown in Fig. 4. All samples were formed in an octahedron-like shape as reported in [11]. In this study, the as-prepared powders showed a dense structure with a very smooth surface. In contrast, the calcined samples had a porous structure assembled from the aligned spherical nanoparticles. The size of the spherical nanoparticles was dependent on the concentration of the doping metal. The reason for this has been clearly described in the previous section. In this study, the porous structures were proposed to be formed via the thermal decomposition of zinc oxalate dihydrate as previously mentioned in the thermal study section.

3.1.4. Optical study

In general, the UV absorption is related to the electronic transition from filled valence states to empty conduction states. In this study, the absorbance of samples was measured as a

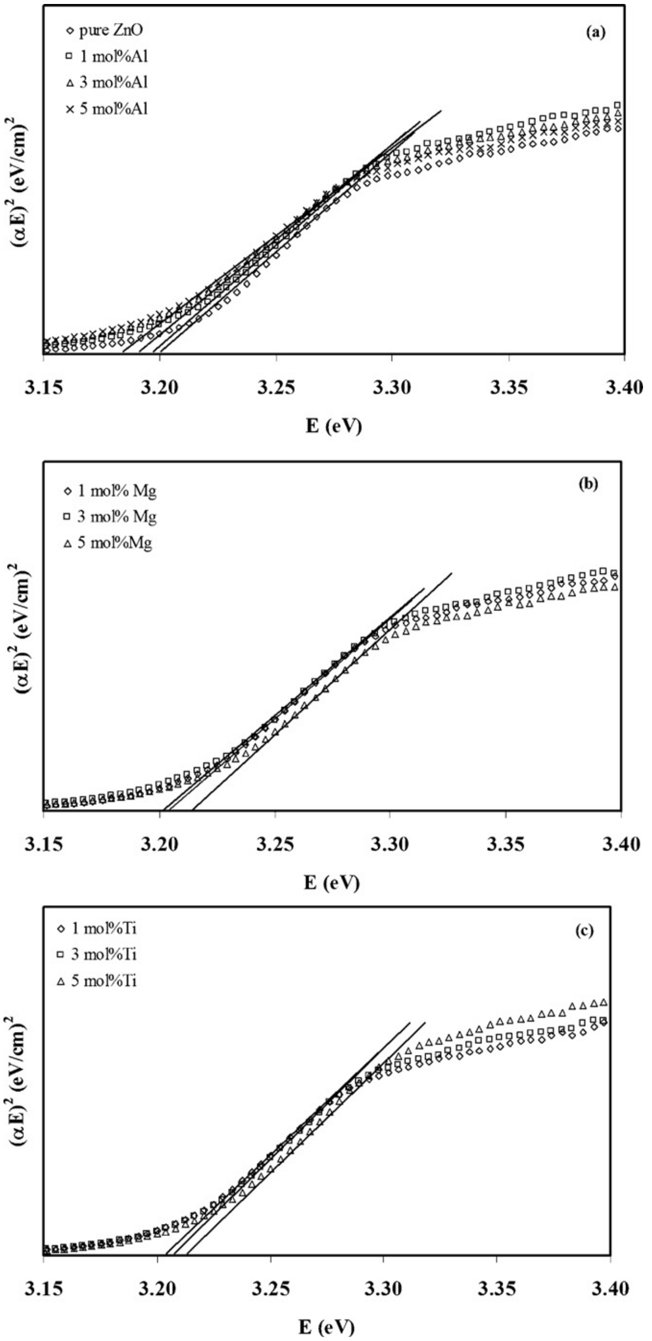

Fig. 5. Evolution of $(\alpha E)^2$ vs. E curves of (a) Al-doped ZnO nanopowders, (b) Mg-doped ZnO nanopowders and (c) Ti-doped ZnO nanopowders.

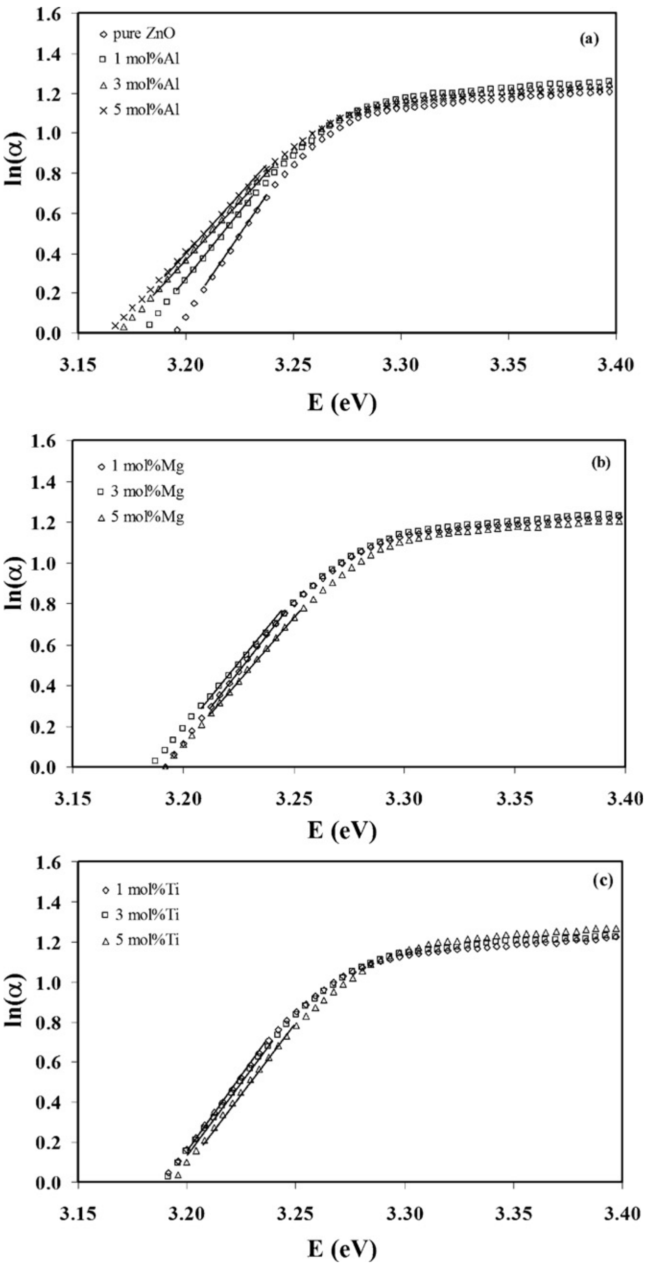

Fig. 6. The plots of ln(α) vs. E for evaluating the defect concentration of (a) Al-doped ZnO nanopowders, (b) Mg-doped ZnO nanopowders and (c) Ti-doped ZnO nanopowders.

function of wavelength in the range of 200–800 nm and all samples showed a highly transparent mode in a visible region.

Based on the absorption spectra, the direct band-gap of all samples could be calculated from the following relationship:

$$(\alpha E) = A(E - E_g)^{n/2} \tag{6}$$

where α is the optical absorption coefficient, E (=hc/λ) is the photon energy, A is a constant, E_g is the direct band gap and $n = 1$ due to ZnO shows a direct transition. Normally, the absorption coefficient (α) can be estimated by the equation:

$$\alpha = \frac{A}{d'} \tag{7}$$

where A is the measured absorbance and d' is the thickness of samples in a UV–vis cell (0.4 cm) and E could be approximated by:

$$E = \frac{1240}{\lambda} \tag{8}$$

where λ is the measured wavelength in nm.

The extrapolation of a linear part of the curve of $(\alpha E)^2$ vs. E to the $\alpha E = 0$ (where $E = E_g$) as shown in Fig. 5 is referred to as a direct band-gap (E_g) of the sample. It could be clearly observed from Table 1 that the E_g value of the Mg- and Ti-doped ZnO nanopowders was strongly dependent upon its crystallite size. In this study, the E_g value of ZnO doped with 1 and 3 mol% of Mg and Ti ions is quite similar because their sizes are not different. A few reports [29,30] have proposed that the optical band-gap also depended on the defect concentration in the ZnO crystal and the nature of disorder in the system is known as a band tailing effect. However, the band tailing effect influences only the Al-doped ZnO nanopowders. In general, the absorption coefficient below the band edge ($E < E_g$) should vary exponentially with the photon energy according to the relationship:

$$\alpha E = \alpha_0 \exp\left(\frac{E}{E_0}\right) \tag{9}$$

where α_0 is the constant and E_0 is an empirical parameter depending on the defect concentration, temperature and structural disorder.

To confirm the statement above, the curves of $\ln(\alpha)$ vs. E were plotted as shown in Fig. 6 and the reciprocal of the slopes referred to the defect concentration is given in Table 1. Noticeably, the defect concentration is in the same range for all Mg- and Ti-doped ZnO nanopowders even though different concentrations of doping metal were used. However, it was observed that Al-, Mg- and Ti-doped ZnO nanopowders occupied more defect concentrations compared to the pure ZnO nanopowders, nevertheless, the wider band-gap values were still obtained for Mg- and Ti-doped ZnO nanopowders. From these results, it could be concluded that the crystallite size strongly influenced the optical band-gap of the Mg- and Ti-doped ZnO nanopowders. In this study, the significant blue-shift occurred when the Mg and Ti ions in the precursor solutions were increased to 5 mol%. This behavior could be explained by the Moss–Burstein band filling effect [6]. Normally, ZnO is an n-type semiconductor, the Fermi level is inside the conduction band and this Fermi level might be located at a higher level for the Mg- and Ti-doped ZnO nanopowders. Since electrons transit from the valence band to the Fermi state, so the absorption edge shifted to the lower wavelength or the blue-shift. In contrast, the E_g value of Al-doped ZnO nanopowders also related to the defect concentration. It was observed that the sample with larger crystallite size and higher defect concentration performed smaller E_g value [31].

4. Conclusions

Porous ZnO, Al-, Mg- and Ti-doped ZnO nanopowders with an octahedron-like shape were successfully constructed from self-assembled nanoparticles by the thermal decomposition method and all samples exhibited a hexagonal wurtzite structure without an impurity phase such as Al_2O_3, MgO and TiO_2. The doping metal ions did not alter the shape of samples but they affected the crystallite size. The crystallite size normally decreased when metal ions were increased as occurred in Mg- and Ti-doped ZnO nanopowders. This evidence can be explained by the Zener pinning effect. Nevertheless, the crystallite size was inversely changed to Al ions concentration. In this study, we proposed that Al ion adhered on the ZnO surface can agglomerate and reduce the efficiency of pinning, giving rise to a growth of crystallite size. The E_g value of metal-doped ZnO nanopowders involved the crystallite size and defect concentration, namely a smaller size and lower defect concentration gave a larger E_g value and the dependence of E_g value on crystallite size can be explained by the Moss–Burstein effect.

Acknowledgements

The authors would like to acknowledge the financial support from the Research, Development and Engineering (RD&E) fund through The National Nanotechnology Center (NANOTEC), The National Science and Technology Development Agency (NSTDA), Thailand (Project no. NN-B-22-FN8-19-52-21) to Prince of Songkla University and the Center for Innovation in Chemistry (PERCH-CIC), Commission on Higher Education, Ministry of Education. The authors also would like to acknowledge Mr. Michael Benjamin Lane for English correction.

References

[1] E.R. Leite, J.A. Cerri, E. Longo, J.A. Varela, C.A. Paskocima, Sintering of ultrafine undoped SnO_2 powder, J. Eur. Ceram. Soc. 21 (2001) 669–675.

[2] L. Sikong, J. Damchan, K. Kooptarnond, S. Niyomwas, Effect of doped SiO_2 and calcination temperature on phase transformation of TiO_2 photocatalyst prepared by sol–gel method, Songklanakarin, J. Sci. Technol. 30 (2008) 385–391.

[3] T. Ahmad, S. Vaidya, N. Sarkar, S. Ghosh, K. Ganguli, Zinc oxalate nanorods: a convenient precursor to uniform nanoparticles of ZnO, Nanotechnology 17 (2006) 1236–1240.

[4] M. Ristic, S. Music, M. Godec, Properties of γ-FeOOH, α-FeOOH and α-Fe_2O_3 particles precipitated by hydrolysis of Fe^{3+} ions in perchlorate containing aqueous solutions, J. Alloys Compd. 417 (2006) 292–299.

[5] M.M. Pakulska, C.M. Grgicak, J.B. Giorgi, The effect of metal and support particle size on NiO/CeO_2 and NiO/ZrO_2 catalyst activity in complete methane oxidation, Appl. Catal. A 332 (2007) 124–129.

[6] S. Suwanboon, A. Amornpitoksuk, A. Haidoux, J.C. Tedenac, Structural and optical properties of undoped and aluminium doped zinc oxide nanoparticles via precipitation method at low temperature, J. Alloys Compd. 462 (2008) 335–339.

[7] Z. Ling, C. Leoch, R. Freer, Heterojunction gas sensors for environmental NO_2 and CO_2 monitoring, J. Eur. Ceram. Soc. 21 (2001) 1977–1980.

[8] C.Y. Hsu, T.F. Ko, Y.M. Huang, Influence of ZnO buffer layer on AZO film properties by radio frequency magnetron sputtering, J. Eur. Ceram. Soc. 28 (2008) 3065–3070.

[9] S.M. Gheno, R.H.G.A. Kiminami, M.R. Morelli, P.I. Paulin Filho, Electric force microscopy investigations of barrier formations in ZnO-based varistors, J. Eur. Ceram. Soc. 30 (2010) 549–554.

[10] Y. Wang, X. Li, N. Wang, X. Quan, Y. Chen, Controllable synthesis of ZnO nanoflowers and their morphology-dependent photocatalytic activities, Sep. Purif. Technol. 62 (2008) 727–732.

[11] J. Zheng, Z.Y. Jiang, Q. Kuang, Z.X. Xie, R.B. Huang, L.S. Zheng, Shaped-controlled fabrication of porous ZnO architectures and their photocatalytic properties, J. Solid State Chem. 182 (2009) 115–121.

[12] X. Wei, D. Chen, Synthesis and characterization of nanosized zinc aluminate spinel by sol–gel technique, Mater. Lett. 60 (2006) 823–827.

[13] M. Salavati-Niasari, N. Mir, F. Davar, ZnO nanotriangles: synthesis, characterization and optical properties, J. Alloys Compd. 476 (2009) 908–912.

[14] Y. Zhang, Y. Liu, L. Wu, H. Li, L. Han, B. Wang, E. Xie, Effect of annealing atmosphere on the photoluminescence of ZnO nanospheres, Appl. Surf. Sci. 255 (2009) 4801–4805.

[15] S. Suwanboon, P. Amornpitoksuk, S. Muensit, Enhancement of optical bandgap and luminescent characteristics of one-dimensional ZnO nanoparticles, J. Ceram. Process Res. 11 (2010) 419–424.

[16] N. Samaele, P. Amornpitolsuk, S. Suwanboon, Effect of pH on the morphology and optical properties of modified ZnO particles by SDS via a precipitation method, Powder Technol. 203 (2010) 243–247.

[17] K. Thongsuriwong, P. Amornpitoksuk, S. Suwanboon, The effect of aminoalcohols (MEA, DEA and TEA) on morphological control of nanocrystalline ZnO powders and its optical properties, J. Phys. Chem. Solids 71 (2010) 730–734.

[18] A. Ishizumi, Y. Takahashi, A. Yamamoto, Y. Kanemitsu, Fabrication and optical properties of Eu^{3+}-doped ZnO nanospheres and nanorods, Mater. Sci. Eng. B 146 (2008) 212–215.

[19] Q. Xiao, S. Huang, J. Zhang, C. Xiao, X. Tan, Sonochemical synthesis of ZnO nanosheet, J. Alloys Compd. 459 (2008) L18–L22.

[20] K.G. Kanade, B.B. Kale, R.C. Aiyer, B.K. Das, Effect of solvents on the synthesis of nano-size zinc oxide and its properties, Mater. Res. Bull. 41 (2006) 590–600.

[21] Z. Jia, L. Yue, Y. Zheng, Z. Xu, Rod-like zinc oxide constructed by nanoparticles: synthesis, characterization and optical properties, Mater. Chem. Phys. 107 (2008) 137–141.

[22] M. Peiteado, A.C. Caballero, D. Makovec, Phase evolution of $Zn_{1-x}Mn_xO$ system synthesized via oxalate precursors, J. Eur. Ceram. Soc. 27 (2007) 3915–3918.

[23] K.G. Kanade, B.B. Kale, J.O. Baeg, S.M. Lee, C.W. Lee, S.J. Moon, H. Chang, Self-assembled aligned Cu doped ZnO nanoparticles for photocatalytic hydrogen production under visible light irradiation, Mater. Chem. Phys. 102 (2007) 98–104.

[24] X. Wei, D. Chen, W. Tang, Preparation and characterization of the spinel oxide $ZnCo_2O_4$ obtained by sol–gel method, Mater. Chem. Phys. 103 (2007) 54–58.

[25] Y.Q. Li, J.L. Wang, S.Y. Fu, S.G. Mei, J.M. Zhang, K. Yong, Facile synthesis of antimony-doped tin oxide nanoparticles by a polymer–pyrolysis method, Mater. Res. Bull. 45 (2010) 677–681.

[26] S. Suwanboon, T. Ratana, T. Ratana, Effects of Al and Mn dopant on structural and optical properties of ZnO thin film prepared by sol–gel route, Walailak, J. Sci. Technol. 4 (2007) 111–121.

[27] S.K. Jayanthi, S. Chawla, Synthesis of Mn doped ZnO nanoparticles with biocompatible capping, Appl. Surf. Sci. 256 (2010) 2630–2635.

[28] R.W. Kelsall, I.W. Hamley, M. Geoghegan, Nanoscale Science and Technology, John Wiley and Sons, West Sussex, 2005.

[29] S. Dutta, S. Chattopadhyay, D. Jana, Annealing effect on nano-ZnO powder studied from positron lifetime and optical absorption spectroscopy, J. Appl. Phys. 100 (2006) 114328.

[30] S. Dutta, M. Chakrabarti, S. Chattopadhyay, D. Jana, Defect dynamics in annealed ZnO by positron annihilation spectroscopy, J. Appl. Phys. 98 (2005) 053513.

[31] S. Suwanboon, P. Amornpitoksuk, P. Bangrak, Synthesis, characterization and optical properties of $Zn_{1-x}Ti_xO$ nanoparticles prepared via a high-energy ball milling technique, Ceram. Int. 37 (2011) 333–340.